Space Weather®

RESEARCH ARTICLE
10.1029/2023SW003523

# Investigating the Interhemispheric Asymmetry in Joule Heating During the 2013 St. Patrick's Day Geomagnetic Storm

**A. R. Smith[1], D. S. Ozturk[1], P. Delamere[1], G. Lu[2], and H. Kim[3]**

[1]Geophysical Institute, University of Alaska, Fairbanks, AK, USA, [2]High Altitude Observatory, NCAR, Boulder, CO, USA, [3]New Jersey Institute of Technology, Newark, NJ, USA

**Key Points:**

- Solar insolation has a significant effect on simulated hemispheric TEC even at equinox
- Asymmetric conductance profiles result in diurnal variation in heating aligned with solar insolation over the magnetic high latitude regions
- Realistic drivers may produce more frequent and intense localized heating events

**Correspondence to:**

A. R. Smith,
asmith155@alaska.edu

**Citation:**

Smith, A. R., Ozturk, D. S., Delamere, P., Lu, G., & Kim, H. (2023). Investigating the interhemispheric asymmetry in Joule heating during the 2013 St. Patrick's Day geomagnetic storm. *Space Weather*, *21*, e2023SW003523. https://doi.org/10.1029/2023SW003523

Received 3 APR 2023
Accepted 24 AUG 2023

**Author Contributions:**

**Conceptualization:** A. R. Smith, D. S. Ozturk, P. Delamere
**Data curation:** G. Lu
**Formal analysis:** A. R. Smith
**Funding acquisition:** D. S. Ozturk, P. Delamere, H. Kim
**Investigation:** A. R. Smith
**Methodology:** A. R. Smith, D. S. Ozturk
**Project Administration:** D. S. Ozturk
**Resources:** G. Lu
**Software:** A. R. Smith
**Supervision:** D. S. Ozturk
**Visualization:** A. R. Smith
**Writing – original draft:** A. R. Smith
**Writing – review & editing:** A. R. Smith, D. S. Ozturk, P. Delamere, G. Lu, H. Kim



**Abstract** Sudden changes in energy input from the magnetosphere during geomagnetic storms could drive extreme variability in the ionosphere-thermosphere system, which in turn affect satellite operations and other modern infrastructure. Joule heating is the main form of magnetospheric energy dissipation in the ionosphere-thermosphere system, so it is important to know when and where Joule heating will occur. While Joule heating occurs all the time, it can increase rapidly during geomagnetic storms. We investigated the Joule heating profile of the 2013 St Patrick's day storm using the University of Michigan Global Ionosphere-Thermosphere Model (GITM). Using empirical and data-assimilated drivers we analyzed when and where intense Joule heating occurred. The timing, location, and sources of interhemispheric asymmetry during this geomagnetic storm are of key interest due to near equinox conditions. Hemispheric comparisons are made between parameters, including solar insolation, total electron content profiles, and Pedersen and Hall conductance profiles, obtained from GITM driven with empirical driven input, versus those driven with data-assimilated patterns. Further comparisons are made during periods of peak hemispheric Joule heating asymmetry in an effort to investigate their potential sources. Additionally, we compare the consistency of the interhemispheric asymmetry between empirical- and data-assimilated driven simulations to further analyze the role of data-assimilated drivers on the IT system.

**Plain Language Summary** Geomagnetic storms manifested by sudden changes in the Earth's magnetic field can affect satellite operations and other infrastructure. Understanding how the energy dissipates in the upper atmosphere is important to predict when and where intense energy will occur. We used a computer model to analyze the energy released during the 17th–18th March 2013 storm. By comparing the model results driven with different inputs, we determined where and when the energy was most intense. We also looked at differences between the Northern and Southern Hemispheres during the storm. Our results provide insight into how storms affect different parts of the upper atmosphere and can help us better prepare for future storms that could affect our technology on Earth.

## 1. Introduction

Magnetospheric processes primarily influence the high-latitude regions of Earth's ionosphere-thermosphere (IT) system, which can further affect the global IT system (Richmond, 2011). While these magnetospheric drivers are present all the time, they only significantly contribute to the variation of the IT system over a period of up to 36 hr, even during storm time (Meng & Verkhoglyadova, 2021). In order to determine the strength of these drivers, Joule heating is used as a measure of the energy deposition into the IT system from the magnetosphere. It has been estimated from empirical relationships, that for a coronal mass ejection (CME) storm, energy input into the Magnetosphere-Ionosphere-Thermosphere (MIT) system on average can be ~71% attributed to Joule heating, ~17% to auroral precipitation, and ~12% to the ring current (Turner et al., 2009). A reason why Joule heating, and energy deposition from the magnetosphere into the IT system in general, is an important area of research is due to the fact that a large number of satellites, including the International Space Station, call the thermosphere home. Atmospheric drag on these satellites may increase rapidly due to increased density at higher altitudes caused by an increase in the thermospheric temperature. Additionally, localized Joule heating events are associated with traveling ionospheric disturbances (TIDs) and traveling atmospheric disturbances (TADs) (Deng et al., 2019). These disturbances carry the localized heating to other parts of the IT system and may cause global perturbations.

Joule heating in the context of MIT coupling is due to the collisional heating between ions and neutrals in the IT system. The rate of this collisional heating can be described by the following equation (Banks & Kockarts, 1973; Schunk, 1975; J. Zhu & Ridley, 2016)

$$Q_J = \sum_k n_k m_k \sum_t \frac{\nu_{kt}}{m_k + m_t}\left[3\kappa(T_i - T_n) + m_t(\boldsymbol{u}_n - \boldsymbol{u}_i)^2\right]. \quad (1)$$

where the subscripts $t$ refers to ions and $k$ refers to neutrals, $\nu_{kt}$ is the ion-neutral collision frequency, $\kappa$ is the Boltzmann constant, $T_n$ and $T_i$ are the neutral and ion bulk temperatures, and $\boldsymbol{u_n}$ and $\boldsymbol{u_i}$ are the neutral and ion bulk velocities respectively. The ion velocity is primarily driven by the convection electric field, which can increase significantly during periods of high geomagnetic activity when a stronger cross polar cap potential is formed. Since Joule heating is a key measure of energy input into the IT system from the magnetosphere, understanding interhemispheric asymmetry of Joule heating can aid in the understanding of interhemsipheric asymmetries in general. However, there are various drivers that can affect interhemispheric asymmetry during geomagnetic storms.

Global numerical simulations allow for the examining the roles of external drivers, as well as giving a more global perspective. Hong et al. (2021) conducted eight numerical experiments to determine the contribution of potential causes of interhemispheric asymmetry. The paper compared simulations where single parameters were changed, such as season, geomagnetic configuration, the magnitude of the IMF $B_y$, and amount of energetic particle precipitation. The paper then looked at the responses in terms of the electron density at 120 km, the neutral mass density and horizontal winds at 300 km, and the hemispheric-integrated Joule heating. Hong et al. (2021) found that seasonal variation of solar irradiance causes substantial asymmetry in all examined parameters. They also reported that the magnetic field configuration results in an asymmetry in all examined parameters, with a significant daily variation but a relatively small daily average asymmetry. The asymmetries in electron precipitation (factor of 2 between northern and southern hemispheres) and the magnitude of the $B_y$ ($\pm$10 nT) component of the interplanetary magnetic field (IMF) used in their study could be smaller than those occurring during a real storm. Hence, the contribution of asymmetric forcing to the IT system may be more important during intense driving (Hong et al., 2021).

In light of these numerical experiments, it may be considered reasonable to assume that the north and south hemispheres in the 2013 Saint Patrick's day geomagnetic storm had very similar ionospheric conductivity profiles. However, even at equinox the solar insolation is not equal between the two magnetic hemispheres. This is due to the asymmetric off set of geomagnetic and geographic poles between the two hemispheres, which results in a diurnal variation in solar insolation over the magnetic hemispheres (Laundal et al., 2016). Although the amount of solar energy that reaches the Earth's magnetic hemispheres can be the same at a particular instant, the way this energy is distributed across these regions is not symmetrical due to the unequal geographic and geomagnetic offset between the two hemispheres. There are other asymmetries in Earth's magnetic field strength which Pakhotin et al. (2020) have shown there is a northern hemispheric preference for electromagnetic energy input, over all seasons, by using Swarm satellite observations of Poynting flux. This has also been observed with DMSP satellites (Knipp et al., 2021). A symmetric, true equinox scenario would require Earth's geomagnetic field to be symmetric in strength and aligned with the rotation axis, similar to Saturn's extremely axisymmetric magnetic field (Cao et al., 2011). Hence, this inherent asymmetry at Earth must be considered.

Modeling studies of the 2013 Saint Patrick's day geomagnetic storm has been used as case study to investigate interhemispheric asymmetries, the role of solar wind driving conditions, and how well models estimate Joule heating. Verkhoglyadova et al. (2017) focused on the energy budget for the 2013 Saint Patrick's day geomagnetic storm. Their goal was to see how well the Global Ionosphere-Thermosphere Model (GITM) captures energy transport in the two storms. Their results indicate that modeled Joule and auroral heating powers at some instances during the storm main phases are similar, despite significant differences in the storms' geomagnetic strengths. They propose that these similarities could be associated with a saturation on the IT heating flux in the model during a storm (Verkhoglyadova et al., 2017). The paper also found that the modeled total auroral heating estimates are comparable to Assimilative Mapping of Ionospheric Electrodynamics (AMIE) based hemispheric power estimates for storms of similar strength, while modeled Joule heating is lower. Also, they found that there is an interhemispheric asymmetry in both the heating and cooling patterns, which begs the question of whether this asymmetry is driven by the solar wind or from lower atmospheric drivers. When comparing to data, their

simulation results indicate that modeled Joule heating and auroral heating can be directly controlled by external driving in the 2013 storm. Furthermore, modeled auroral heating is approximately equivalent to modeled Joule heating and does not show a clear dependence on minimum *Dst*.

While empirical drivers for global circulation models (GCMs) have been commonly used, there is a need to move toward realistic, data-assimilated drivers. Using data-assimilated drivers will include meso-scale physics and potentially fill in missing particle precipitation and Joule Heating (Cosgrove & Codrescu, 2009; Ozturk et al., 2020). Meso-scale Joule heating is a first-order effect for the thermospheric energy budget, and cannot be captured well by empirical drivers (Codrescu et al., 2000). In addition, utilizing data-assimilated drivers in GCMs potentially allows for capturing localized Joule heating events caused by neutral winds (Thayer, 1998). In general, this will lead to better understanding of MIT coupling and improve modeling capabilities (Burns et al., 2007; Heelis & Maute, 2020). Specifically, using GITM with a data-assimilated driver will potentially improve model capabilities for estimating Joule heating variability, reducing the differences between estimates from different methods (Heelis & Maute, 2020; Kalafatoglu Eyiguler et al., 2018).

Low- to mid-latitude region investigations of the 2013 Saint Patrick's day storm using data-assimilated drivers in GITM can be found in Q. Zhu, Lu, Maute, et al. (2022) and Q. Zhu, Lu, and Deng (2022). In this study we focus solely on the mid- to high-latitude regions during 2013 Saint Patrick's Day geomagnetic storm and use Joule heating to determine the extent of hemispheric asymmetry. We use both empirical and data-assimilated drivers for modeling the event and focus on the role of solar insolation on hemispheric asymmetries, building on the understanding of this event from Verkhoglyadova et al. (2017). We will first introduce GITM and the modeling setup and inputs used in this study. Then we present the modeling results, and address the main findings of this study and potential future work to be done.

## 2. Methods

### 2.1. Global Ionosphere-Thermosphere Model

The University of Michigan's Global Ionosphere-Thermosphere Model (GITM) is a three-dimensional first-principle general circulation model simulating the ionosphere-thermosphere of Earth, Mars, and Titan. It explicitly solves for the temperatures, velocities, and densities of ions, electrons, and neutrals in a global spherical coordinated system (Ridley et al., 2006). To allow for the propagation of acoustic waves, GITM relaxes the hydrostatic assumption (Deng et al., 2008, 2011; Lin et al., 2017; Zhao et al., 2020; Q. Zhu et al., 2017), providing a more accurate description of high-frequency gravity wave propagation (Deng & Ridley, 2014). GITM typically updates the electric field every minute, but it could be driven with higher temporal resolution if the application requires it (Deng & Ridley, 2007). GITM also includes a self-consistent electrodynamo solver for the mid- and low-latitudes (Vichare et al., 2012).

To investigate the role of realistic drivers in IT modeling and hemispheric asymmetries, this study uses two different methods to provide the high-latitude electric potential and auroral precipitation to simulate the IT responses to the geomagnetic storm. The first method uses empirical models and the second method uses a realistic model. For the empirical models, the Weimer model (Weimer, 2005) for high-latitude electric potential and Fuller-Rowell Evans model (Fuller-Rowell & Evans, 1987) for auroral precipitation patterns were used to drive GITM simulations. The input for the Weimer model was 1 min resolution IMF and solar wind data from the NASA OMNI database. The Weimer model flips the sign of $B_y$ for modeling the southern hemisphere and accounts for the dipole tilt angle as well (Weimer, 2005). Any data gaps were filled with linear interpolation. Specifically, the data used in this study is the IMF in GSM coordinates, solar wind $v_x$, $v_y$, $v_z$, and density. NOAA hemispheric power indices were used as an input to the Fuller-Rowell Evans model. For briefness, the simulations driven by these two empirical models will be referred to as the Weimer-FRE driven simulation.

For the data-assimilated driver, the Assimilative Mapping of Ionospheric Electrodynamics (AMIE) (Lu, 2017; Richmond, 1992) input data replaced the Weimer model and Fuller-Rowell Evans model for high-latitude electric potential and auroral precipitation patterns respectively. AMIE is a process to globally estimate time varying quantities of high-latitude ionospheric electrodynamics fields by synthesizing various ground- and space-based observations. In this study, the high-latitude electric potential and auroral precipitation inputs are derived from ground-based and satellite measurements. For the ground-based measurements, 217 magnetometers (with 173 in the northern hemisphere and 44 in the southern hemisphere) and line of sight velocity observations from both

hemispheres from the Super Dual Auroral Radar Network (SuperDARN) were used; for the satellite-based measurements, AMPERE magnetic field perturbations and auroral energy flux, ion drifts, and conductances from the DMSP F16, F17, and F18 satellites were used.

### 2.2. Setup of Simulations

We used GITM to simulate the 2013 Saint Patrick's day geomagnetic storm with the two different upper boundary conditions previously discussed. For both simulations we used a global stretched grid with 2° geographic latitude by 2° geographic longitude and 54 altitude layers ranging from 100 to 600 km. To compute the solar irradiance we used the daily $F_{10.7}$ and the simulations used the APEX geomagnetic coordinate system (Richmond, 1995). While the electric potential and auroral precipitation were updated every minute for the Weimer-FRE driven simulation and every 5 min for the AMIE driven simulation, the outputs of the simulations have a temporal resolution of 5 min during the storm. The International Reference Ionosphere (IRI) and Mass-Spectrometer-Incoherent-Scatter (MSIS) model were used to initialize the ionosphere and thermosphere respectively (Bilitza et al., 2017; Hedin et al., 1977). The Horizontal Wind Model (HWM) was used for the lower boundary of the simulation (Drob et al., 2015). The simulations began on 15th March allowing for 2 days and 6 hr of start up time before the onset of the storm. This allows for the system to become quasi-steady state under quite time conditions. The AMIE driven simulation startup was driven with Weimer-FRE until 17th March, 00:00 UT. Figure 1 shows some of the key input parameters to the Weimer-FRE driven simulation. The 2013 storm has the following progression:

- First Main Phase (17 March 2013, 06:00–14:00 UT),
- Second Main Phase (17 March 2013, 14:00–23:59 UT),
- Recovery Phase (after 18 March 2013, 00:00 UT).

The main phases are distinguished by the increased solar wind and IMF variability (Figures 1a–1c) in the first main phase (M1) compared to the second main phase (M2), as well as a relatively constant Sym-H index (Figure 1e) in the second main phase. Additionally, the dynamic pressure (Figure 1d) in the first main phase is higher and more dynamic than the second. NOAA hemispheric power (Figure 1f) is more elevated in the second main phase compared to the first main phase. Solar insolation (Figure 1g) also varies between the two phases; in the first main phase solar insolation is stronger in the southern hemisphere, while in the second main phase there is a period when solar insolation is higher in the northern hemisphere and a period where it is higher in the southern hemisphere. The transition to the recovery phase (R) is marked by a transition to positive $B_z$ and steadily increasing Sym-H.

The solar insolation in Figure 1g is found by calculating the effective illuminated area of a cell in geographic coordinates, based on the solar zenith angle at 100 km altitude and surface area of the cell. The total shadow areas of the northern and southern hemispheres, above |50°| magnetic latitude, is then multiplied by the solar flux, accounting for the variation of sun-earth distance.

## 3. Results

Figures 2 and 3 show the time series of integrated IT parameters from the two simulations. Cross polar cap potential (CPCP) is the difference between the minimum and maximum potential values above |50°| magnetic latitude. Electron energy flux was integrated above |50°| magnetic latitude and the area-weighted average TEC was calculated over this region as well. Hemispheric Joule heating in the context of this study is the total power imparted to the thermosphere from ion collisional heating. Joule heating was integrated above |50°| magnetic latitude and Joule heating is found over each cell using the following equation

$$P_{JH} = \int Q_J c_p \rho_n dV, \tag{2}$$

where $Q_J$ is the Joule heating rate in Kelvin per second, $c_p$ is the specific heat, and $\rho_n$ is the neutral density. It is noted that in GITM, the auroral heating rate is a representation of the amount of energy deposited into the neutral atmosphere based on an empirical aurora spectrum, and is estimated for each model grid cell. The resultant ion-neutral chemistry from auroral precipitation causes thermal effects that contribute to chemical heating. As a result, the total energy calculated in each grid cell in GITM due to auroral particle precipitation is composed of the auroral heating term and a contribution to the chemical heating term (Rees, 1989; Verkhoglyadova et al., 2017). Auroral heating ($P_{AH}$) was found using the same method in Equation 2 using the auroral neutral heating rate ($Q_A$).

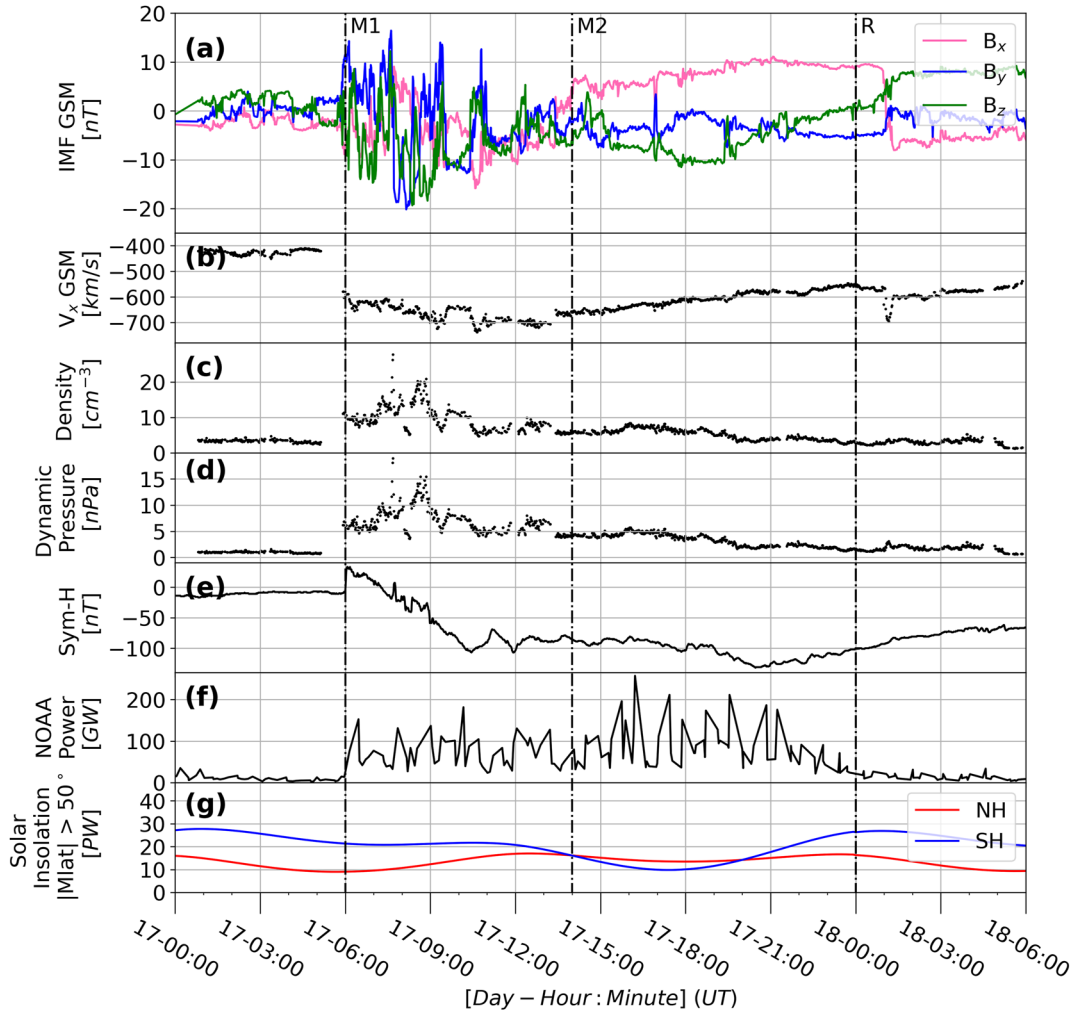


**Figure 1.** An overview of some selected parameters for the 2013 Saint Patrick's day storm. (a) The components of the IMF magnetic field in GSM coordinates; (b) the $v_x$ component of the solar wind velocity; (c) solar wind density; (d) Sym-H; (e) NOAA hemispheric power index; (f) solar insolation for northern hemisphere in red and southern hemisphere in blue above |50°| magnetic latitude. The start of the first main phase (M1), second main phase (M2), and recovery phase (R) are shown by the vertical dot-dash lines.

For the Weimer-FRE driven simulation, the CPCP is the same in both hemispheres, and generally higher than the CPCP for the AMIE driven simulation, as shown in Figures 2a and 3a respectively. The AMIE driven simulation has higher total electron energy flux, Joule heating, and auroral heating during the storm compared to the Weimer-FRE driven simulation, as shown in Figures 2b, 2d, 2e, 3b, 3d, and 3e respectively. The AMIE driven simulation has a more asymmetric peak average TEC response to the storm, with the maximum average TEC of 19.5 TECU in the northern hemisphere and 25.7 TECU in the southern hemisphere, compared to the Weimer-FRE driven simulation, with the maximum average TEC of 20.8 TECU in the northern hemisphere and 23.9 TECU in the southern hemisphere, as shown in Figures 2c and 3c respectively. However, over the duration of the storm, the AMIE driven simulation has a more symmetric TEC response, with the average TEC of 14.8 TECU in the northern hemisphere and 12.3 TECU in the southern hemisphere, compared to the Weimer-FRE driven simulation, with the average TEC of 15.8 TECU in the northern hemisphere and 11.8 TECU in the southern hemisphere. Both simulations see more Joule and auroral heating in the southern hemisphere during the first main phase and in the second half of the second main phase, as well as more Joule and auroral heating in the northern hemisphere in the first half of the second main phase.

Figures 4 and 5 show hemispheric snapshots, with the location of the solar terminator, the potential, height-integrated Joule and auroral heating, Pedersen and Hall conductance profiles, and TEC in geomagnetic local time coordinates. These snapshot are different times (08:00 UT for Figure 4 and 16:00 UT for Figure 5) in order to show some of the

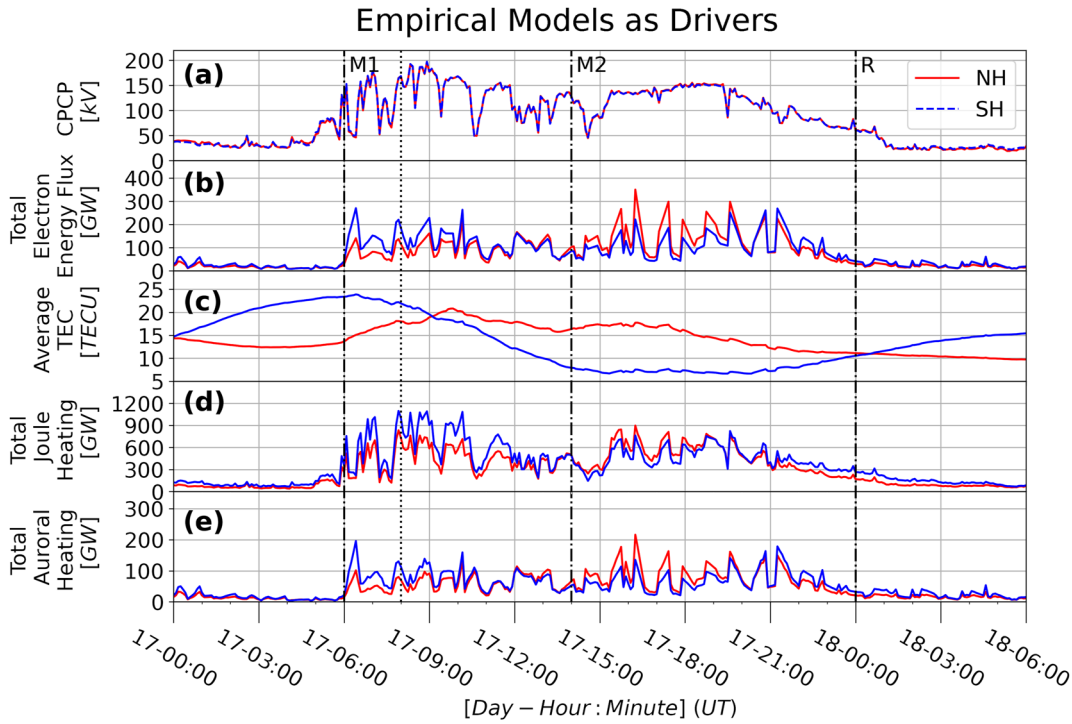


**Figure 2.** An overview of the simulation results for the 2013 Saint Patrick's day storm from Weimer-FRE driven simulations. Time series are taken from values above |50°| magnetic latitude, northern hemispheric values are in red and southern hemispheric values are in blue. In panel (a) is cross polar cap potential and (b) is total electron energy, these are from the driving models. In panel (c) is average TEC, (d) is total Joule heating, and (e) is total auroral heating. The vertical dotted line corresponds to the snapshot time in Figure 4. The start of the first main phase (M1), second main phase (M2), and recovery phase (R) are shown by the vertical dot-dash lines.

qualitative differences between the AMIE and Weimer-FRE driven simulations, as well as the differences in solar insolation. AMIE asymmetric potential patterns can create strong potential gradients (Figure 5b) even with smaller cross polar cap potential as compared to Weimer, which results in significant localized heating events such as the one in Figure 5d in the dusk sector. The conductance profiles, Figures 4 and 5g–5j, show higher conductances above |60°| magnetic latitude in the larger portion of the dayside magnetic hemisphere, especially in the noon to dawn sector.

Simulated TEC was specifically investigated in regions corresponding to West Greenland (67°N–87°N and 45°W–75°W), the geographically conjugate location in Antarctica (67°S–87°S and 45°W–75°W), and over most of Alaska (57°N–75°N, 141°W–175°W) in order to compare with Madrigal GNSS Receiver Network TEC data as seen in Figures 6 and 7 (Rideout & Coster, 2006; Vierinen et al., 2015). These regions were chosen for both interhemispheric comparisons and data availability. As seen in Figure 8, simulated TEC and neutral density were also extracted along the Gravity field and Ocean Circular Explorer (GOCE) satellite's path for further data-model comparisons looking at neutral response (March, Doornbos, & Visser, 2019; March, Visser, et al., 2019).

## 4. Model-Data Comparison

Madrigal GNSS TEC data was used to investigate simulation performance of storm time electron variability. Table 1 shows the root-mean-squared error between simulation results and Madrigal data from the time series in Figure 7, and this shows that AMIE driven simulation preforms better than the Weimer-FRE driven simulation in the TEC comparison. Between around 19:00 and 22:00 UT Madrigal data shows the reported tongue of ionization event (Dang et al., 2019; Shreedevi et al., 2020; Yue et al., 2016) in the southern hemisphere in the noon to dusk sector, Figure 6b, while the simulations underestimate the TEC during this time. The smaller intensity and spacial extent of the simulated TOIs in the southern hemisphere could be the result of sampling bias, resulting in the descepency between the simulations and observations.

Both simulations preform very similarly compared to TEC from GOCE and Madrigal along GOCE's path above |50°| geographic latitude in Figures 8a and 8b, as well as neutral density from the GOCE in Figures 8c and 8d. The

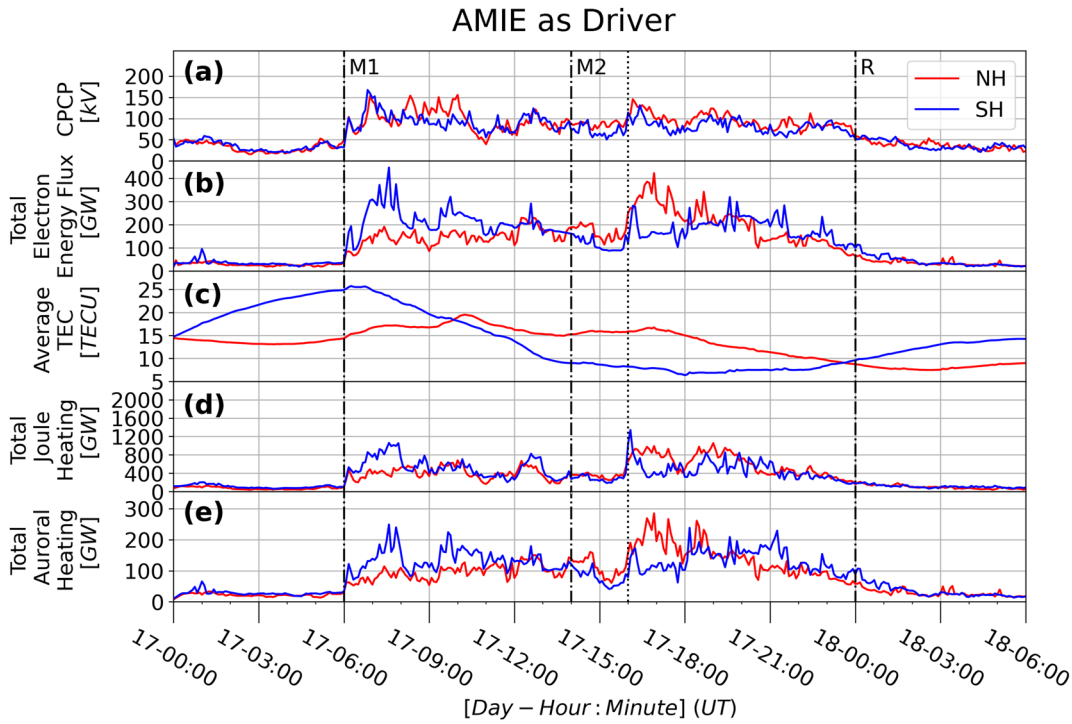


**Figure 3.** An overview of the simulation results for the 2013 Saint Patrick's day storm from AMIE driven simulations. Same format as Figure 2, and the vertical dotted line corresponds to the snapshot time in Figure 5.

simulated TEC results in the northern hemisphere from 11:00 to 18:30 UT are overestimated by the simulations, whereas in the SH the simulated TEC values are comparable to the data. Due to uncertainties in the calibration of GOCE neutral density, the magnitude of the density may be offset from the true value, so the focus of the neutral density comparison should be on the change in neutral density. Both simulations underestimate neutral density as compared to GOCE, though both GOCE observations and the simulations show higher neutral densities in the northern hemisphere as compared to the southern hemisphere. This is likely due to the orbit being located mainly on the night side for the northern hemisphere pass and the on dayside for the southern hemisphere pass. The simulations do follow GOCE's patterns of increasing and decreasing neutral density.

For the purpose of exploring how well the simulations capture MIT energy transfer, which primarily results in Joule heating, the CPCP for both simulations is compared to two other empirical estimates of CPCP, in Figure 9. One is based on the Polar Cap (PC) index derived from ground magnetometers (Ridley & Kihn, 2004) and the other is derived from solar wind parameters (Ridley, 2005). The CPCP derived from SuperDARN data is also shown in Figure 9, and it is on average the lowest measure of CPCP compared here, especially in the southern hemisphere. It is noted that SuperDARN data was used as one of the inputs into AMIE. While AMIE's and Weimer's CPCP is comparable to the solar wind derived CPCP, at times they are lower than the CPCP derived from the polar cap index by a factor of two at times. Since Weimer electric potential patterns are hemispherically symmetric, any interhemispheric asymmetries in Joule heating would be the result of $B_y$ variations or other external factors, such as asymmetric preconditioning or solar insolation.

## 5. Discussion

### 5.1. Solar Wind and IMF Drivers

The solar wind and IMF serve as the primary external drivers of the MIT system and the variation of these parameters during the storm time can be seen in Figures 1a–1c. The peak southward IMF $B_z$ of −20 nT is in the first main phase, then levels out at lower values ($0 < B_z < -11$ nT) for the second main phase. Also, peak $v_x$ and solar wind density occur in the first main phase, then drop to more uniform values in the second main phase, but are still elevated compared to pre-storm values.

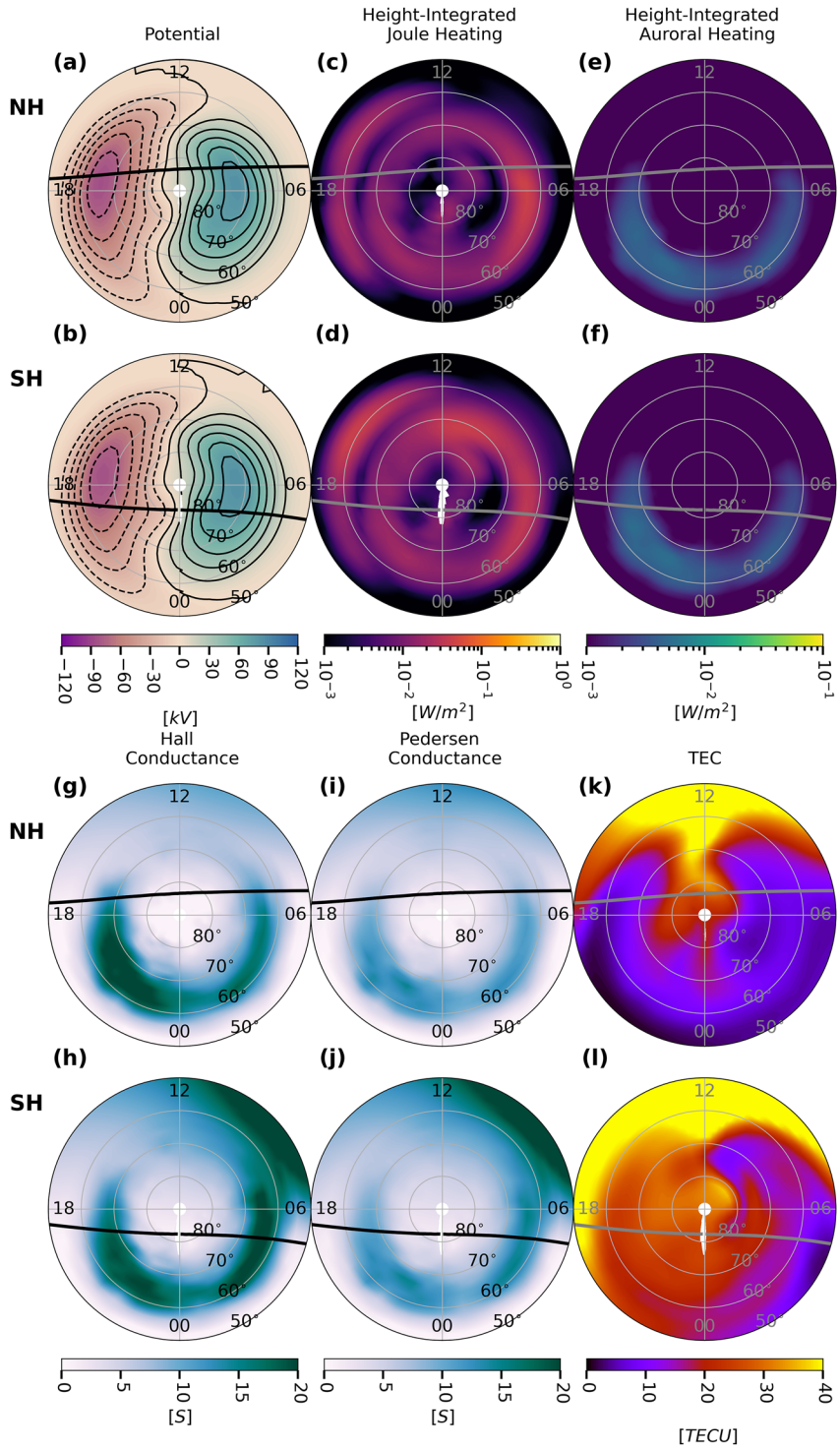


**Figure 4.** Snapshot from the 17th of March, 08:00 UT of the northern hemisphere (top plot) and the southern hemisphere (bottom plot) high latitude regions in magnetic coordinates from the Weimer-FRE driven simulation, with the solar terminator in black. The potential patterns are in panels (a, b) with contour lines every 15 kV. The maximum and minimum values of the two cell potential in the northern hemisphere (a) are 84.1 and −84.2 kV, and in the southern hemisphere (b) the maximum and minimum values are 83.5 and −85.1 kV. Panels (c, d) show height-integrated Joule heating, (e, f) show height-integrated auroral heating, (g, h) show Hall conductance, show (i, j) Pedersen conductance, show (k, l) total electron content (TEC).

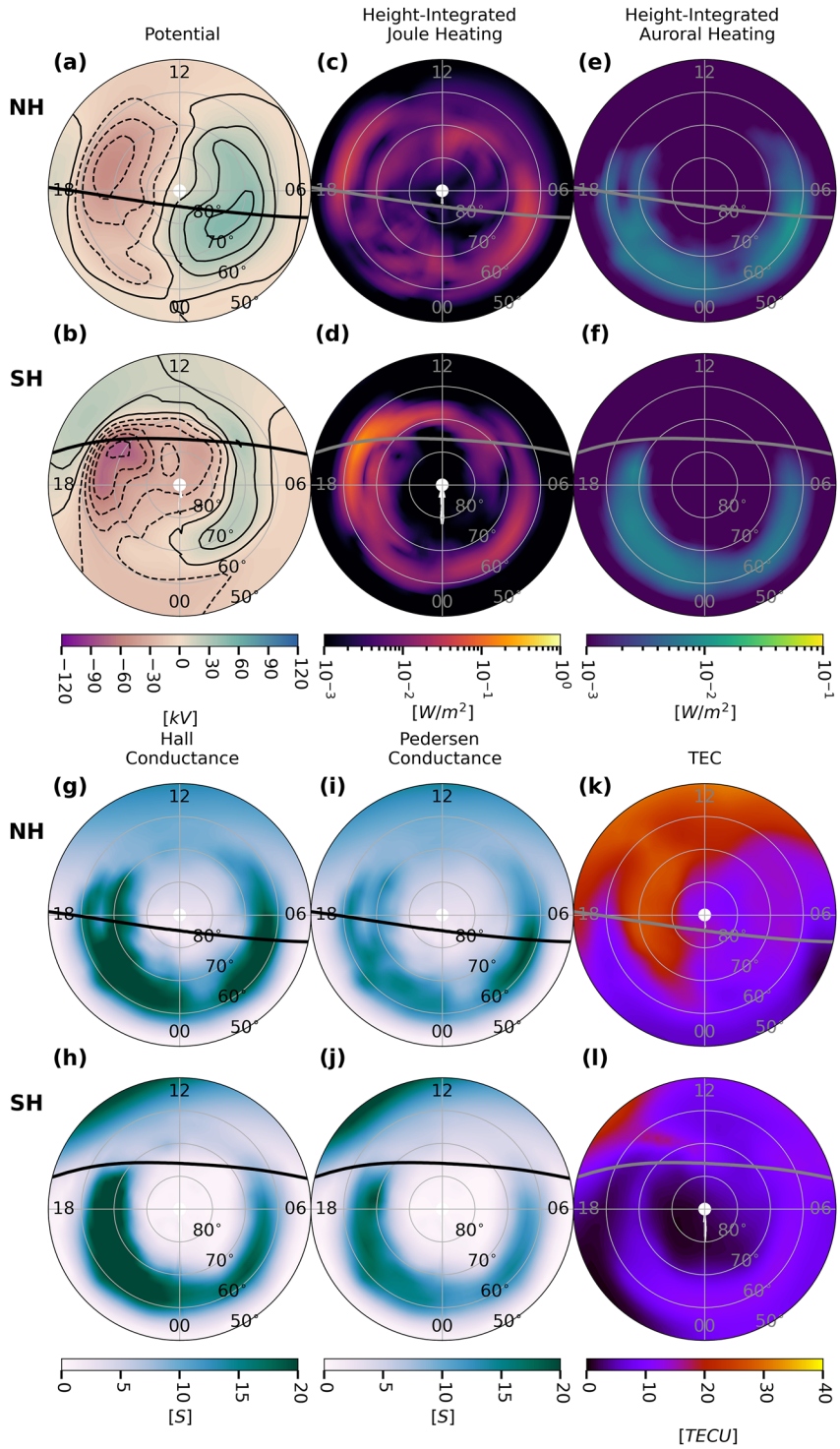


**Figure 5.** Snapshot from the 17th of March, 16:00 UT of the northern hemisphere (top plot) and the southern hemisphere (bottom plot) high latitude regions in magnetic coordinates from the AMIE driven simulation. Same format as Figure 4. The maximum and minimum values of the two cell potential in the northern hemisphere (a) are 50.4 kV and −56.7 kV, and in the southern hemisphere (b) the maximum and minimum values are 31.9 and −82.9 kV.

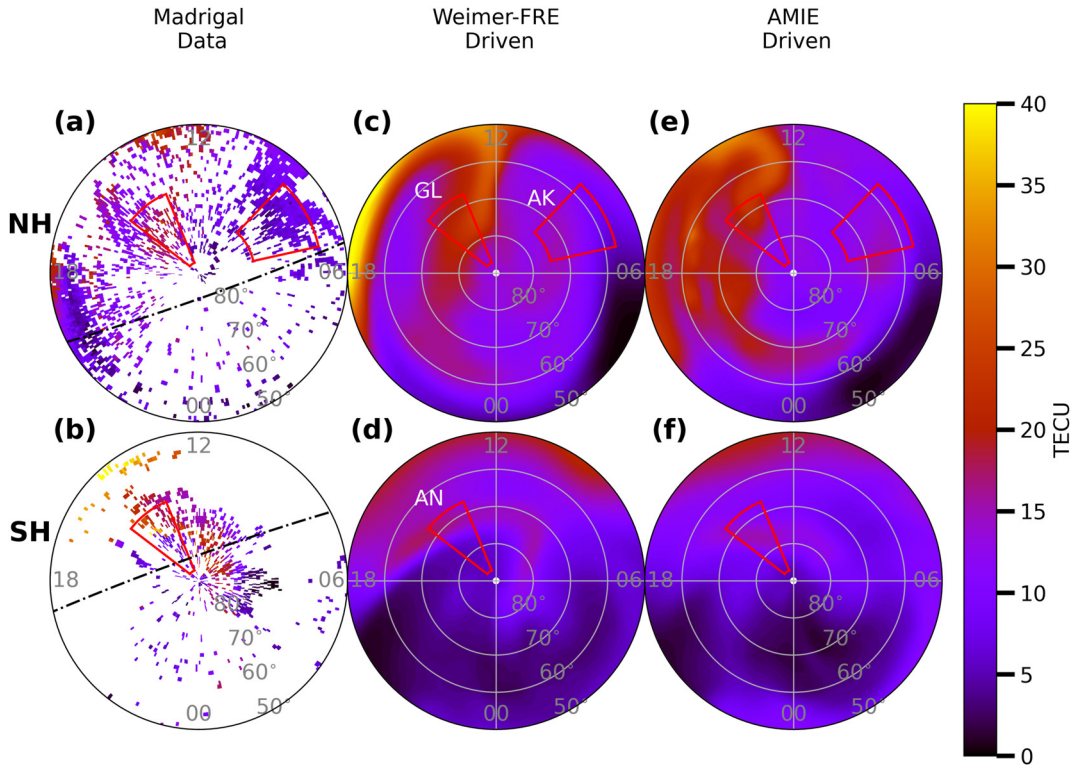


**Figure 6.** Hemispheric TEC profiles from the 17th of March, 18:30 UT of the northern hemisphere (top plot) and the southern hemisphere (bottom plot) high latitude regions in geographic coordinates from Madrigal GNSS Receiver Network data in panels (a, b), Weimer-FRE driven simulation in panels (c, d), and AMIE driven simulations in panels (e, f). The red boxes correspond to the regions where averages are being taken for Figure 7. GL corresponds to Greenland, AN to Antarctica, and AK to Alaska. The dotted-dashed line in (a, b) shows the sun-synchronous orbital path of the GOCE satellite during the storm.

The IMF $B_y$ component is known to cause significant interhemispheric asymmetries. For the 2013 Saint Patrick's day geomagnetic storm, $B_y$ is mainly negative over the full duration of the storm, though in the first main phase there are two periods where $B_y$ is mostly positive for greater than a half hour (06:00–07:45 UT and 08:40–9:30 UT). Outside of this period, $|B_y| < 5$ for a majority of the event. During periods of southward $B_z$, a positive $B_y$ increases average height-integrated Joule heating in the northern hemisphere (McHarg et al., 2005). Figure 10 shows the absolute value of the potential in the dawn and dusk cells from both simulations. While Weimer potential patterns show the expected dawn-dusk asymmetries due to $B_y$ variations, AMIE potential patterns show larger dawn-dusk asymmetries that are frequently opposite the expected due to $B_y$ variations. The difference in hemispheric ion convection, caused by asymmetric electric fields, as measured by the CPCP due to the IMF $B_y$ component's effect on the drivers is then small in Weimer's case or not observed in AMIE's case. The effect of the IMF $B_y$ component on Joule heating asymmetries is not clearly seen during these times in either simulation.

The IMF $B_z$ has a stronger effect on the CPCP and Joule heating in the Weimer-FRE driven simulations as compared to the AMIE driven simulation. There is little asymmetry in the Weimer CPCP, which then cannot account for the asymmetry in Joule heating. For the AMIE driven simulation, which has a more asymmetric CPCP, there are periods of time (such as 08:00–10:00 UT) where there is more Joule heating in the hemisphere with a lower CPCP. This could be explained by differences in conductivity, neutral density, or steeper potential gradients, despite a lower CPCP. We refer the readers interested in these profiles to the data repository.

### 5.2. Solar Insolation

The solar insolation of the atmosphere directly contributes to the conductivity of the polar caps, and during equinox both hemispheres have been assumed to have similar conductivity profiles (Verkhoglyadova et al., 2017). However, due to the difference between the rotation axis and geomagnetic pole locations, even during equinox,

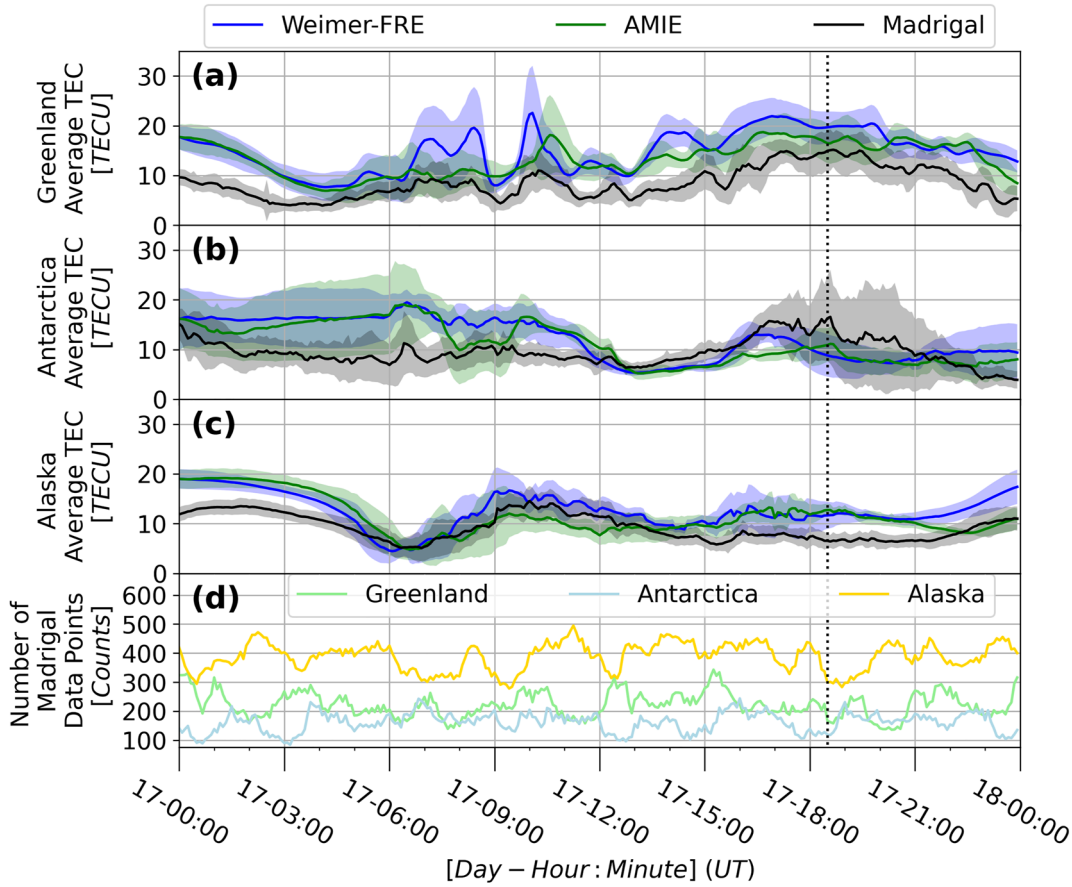


**Figure 7.** Area-weighted average TEC values in (a) Greenland, (b) Antarctica, and (c) Alaska, where these regions correspond to the outlined in Figure 6. The Weimer-FRE driven simulation in blue, the AMIE driven simulation in green, and Madrigal GNSS Receiver Network TECU in black. The shaded region represents one standard deviation of the average. Panel (d) shows the number of grid points with data from Madrigal within the regions of Greenland, Antarctica, and Alaska. The vertical dashed line corresponds to the snapshot time in Figure 6.

the hemispheric conductivity profiles are not the same (Laundal et al., 2016). During the 2013 Saint Patrick's Day geomagnetic storm, the solar insolation above |50°| magnetic latitude in both hemispheres can be seen in Figure 1g. There is a solar insolation bias for the southern magnetic hemisphere over the majority of the storm, with the exception of a period from about 14:00 to 20:00 UT when the northern magnetic hemisphere has more insolation.

Looking at the electromagnetic energy inputs into the thermosphere in Figures 2, 3b, 3d, and 3e and solar insolation during the storm in Figure 1g, both simulations see higher levels of electron energy flux, Joule heating, and auroral heating in the southern hemisphere when there is more solar insolation in the southern hemisphere (06:00–14:00 UT and 20:00–23:59 UT). There are higher levels of electron energy flux, Joule heating, and auroral heating in the northern hemisphere during the period when there is more solar insolation over that hemisphere (14:00–20:00 UT). This is even true in the AMIE simulation, where during most of this period there is a lower cross polar cap potential in the southern hemisphere than in the northern hemisphere. This asymmetry in heating and electron energy flux could be explained by the solar insolation, which increases the conductivity of the ionosphere. With this higher conductivity, the model then allows for more efficient heating in the auroral region.

### 5.3. Interhemispheric Asymmetries

In both simulations, TEC differs between the hemispheres by a factor of two for an extended period, while significant asymmetries exist in the conductance profiles. For example, the AMIE driven simulation exhibits elevated Pedersen conductance in the dawn-midnight sector of the northern hemisphere and elevated conductance levels in the dusk-midnight sector of the southern hemisphere in Figures 5i and 5j. These asymmetries in the conductance

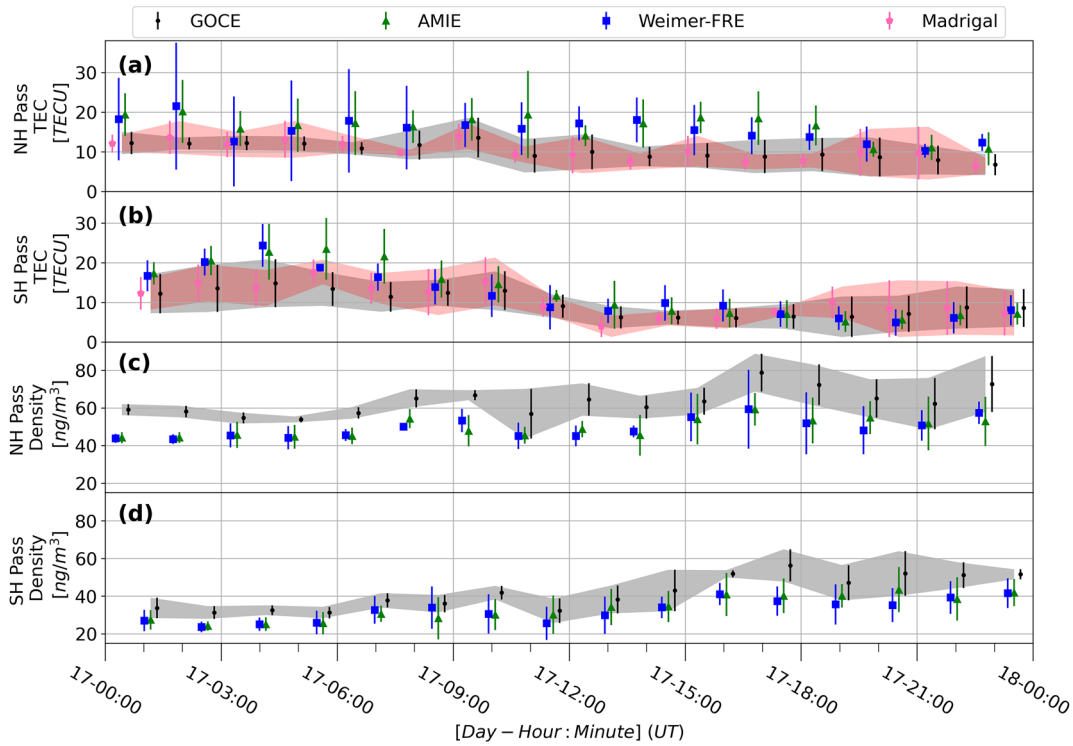


**Figure 8.** GOCE and Madrigal Data and simulation output from along GOCE's path broken into northern hemisphere and southern hemisphere passes above |50°| geographic latitude, see Figure 6 panels (a, b) for the trajectory of these passes. Error bars show one standard deviation of values in each pass. The scatter points are offset from each other for visibility purposes, where the center of each cluster is located halfway through the hemispheric pass.

profiles contribute to the creation of asymmetric neutral heating. Moreover, the AMIE driven simulation shows stronger interhemispheric asymmetries in Joule heating, with the maximum asymmetry in the southern hemisphere being 705 GW more Joule heating than the northern hemisphere at 07:35 UT during the first main phase, while the northern hemisphere has 658 GW more Joule heating than the southern hemisphere at 16:40 UT during the second main phase. On the other hand, the Weimer-FRE driven simulation shows the maximum difference of the southern hemisphere's from the northern hemisphere's Joule heating of 369 GW at 10:10 UT and a maximum difference of the northern hemisphere from the southern hemisphere of 143 GW at 15:25 UT. In both simulations, these maximum asymmetries in Joule heating are aligned with the solar insolation asymmetry. Overall, these simulations demonstrate significant interhemispheric asymmetries in TEC, conductance profiles, and heating profiles even at near equinox conditions.

Figure 4 exemplifies the interhemispheic asymmetries in the Weimer-FRE driven simulation. While the CPCP and potential patterns are symmetric, there is increased TEC, conductivity, and Joule heating in the more sunlight southern hemisphere. The AMIE driven simulations follow this trend, but the data-assimilated potential patterns allow for localized heating events. In the second main phase of the storm, there are higher levels of TEC, conductivity, and Joule heating in the northern hemisphere. However, for a brief time in the southern hemisphere the potential patterns generate a steep gradient which creates a localized heating event, seen in Figure 5d.

**Table 1**
*Model-Data Root-Mean-Squared Error Calculated Between Madrigal TEC and the Simulated Values From the Time Series in Figure 7*

| Location | Weimer-FRE | AMIE |
|---|---|---|
| Greenland | 6.77 TECU | 5.22 TECU |
| Antarctica | 5.37 TECU | 4.96 TECU |
| Alaska | 3.81 TECU | 3.75 TECU |

### 5.4. AMIE and Weimer-FRE Driven Simulations

Overall, the Weimer-FRE and AMIE driven simulations show similar trends in the parameters shown in Figures 2 and 3. Both simulations produce Joule heating of the same order of magnitude, though the Weimer-FRE driven simulation has a larger Joule heating in the first main phase compared to its second main phase and the AMIE driven simulation's first main phase. The AMIE driven simulation's second main phase saw more Joule heating than its first main phase and the Weimer-FRE driven second main phase. The AMIE

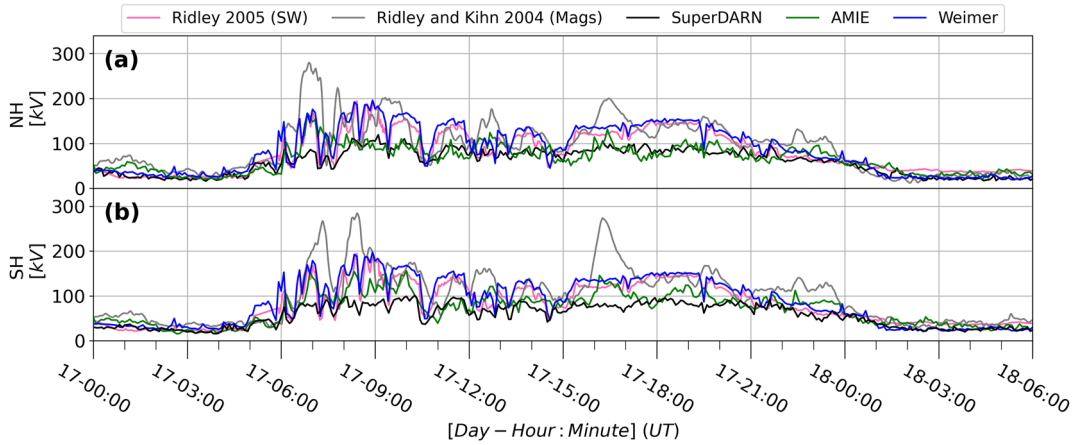


**Figure 9.** Cross Polar Cap Potential (CPCP) in the northern hemisphere (a) and southern hemisphere (b). In pink is the CPCP derived from solar wind parameters (Ridley, 2005), in gray is the CPCP derived from ground magnetometers and the polar cap index (Ridley & Kihn, 2004), in black is the CPCP derived from SuperDARN measurements, in green is CPCP from AMIE, and in blue is CPCP from Weimer.

driven simulation resulted in higher electron energy flux and auroral heating compared to the Weimer-FRE driven simulation. AMIE's ability to resolve localized structures, hence sharper gradients resulted in more localized heating events while performing as well as or better than Weimer-FRE in data model comparisons. Capturing localized heating events is important for IT modeling, as it opens up the possibility for more realistic modeling of TIDs and TADs. Data-assimilated drivers perform as well as or better than empirical drivers in our data-model comparisons, as seen in Figures 6–9 and discussed in Section 4, while being able to produce more of the observed temporal variability.

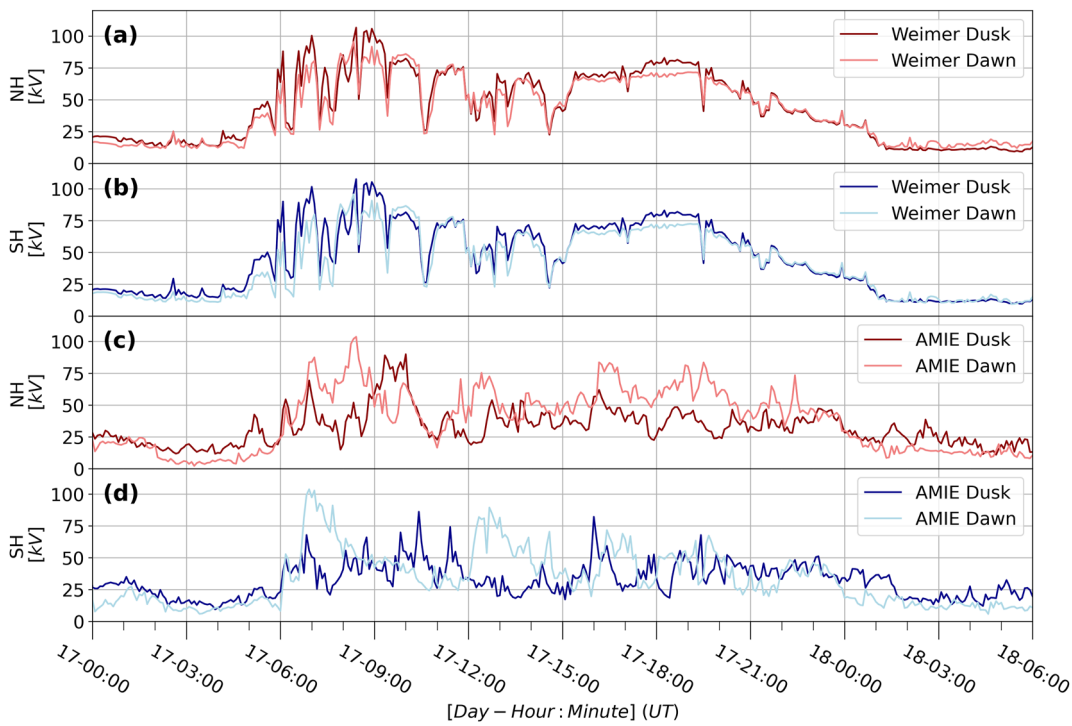


**Figure 10.** Comparisons of the potential in the dusk (minimum value), and dawn (maximum value) cells. From Weimer in the northern hemisphere (a) and southern hemisphere (b), and AMIE in the northern hemisphere (c) and southern hemisphere (d). Northern hemispheric values are in red, and southern hemispheric values are in blue, with the darker shade representing the dusk values and the lighter shade representing the dawn values.

### 5.5. Future Directions for Investigating Sources of Asymmetries in Joule Heating Between Hemispheres

This study focuses on just the 2013 Saint Patrick's day geomagnetic storm, adding insight to the event and using both realistic and empirical drivers. The natural next step would be to extend this methodology to the 2015 Saint Patrick's Day storm. The 2013 and 2015 Saint Patrick's Day geomagnetic storms coincidentally start around the same time interval, providing a unique opportunity to focus on external drivers (Xu et al., 2017). The two storms occurred during the same solar illumination conditions, near equinox on the same day of the year, and began within roughly an hour of each other, meaning that the storms had roughly the same geomagnetic field configuration. Providing a more quantitative comparison between solar illumination, cross polar cap potential, and IMF $B_z$ and $B_y$ and the total hemispheric Joule heating for both the 2013 and 2015 geomagnetic storms would improve the understanding of the role each of these drivers has for determining hemispheric Joule heating. However, hemispheric differences shown in AMIE driven simulation results may be due to the difference in data coverage between the two hemispheres. Installing and using more ground based instruments in the southern hemisphere that could be assimilated into drivers would be beneficial, such as the autonomous adaptive low-power instrument platform (AAL-PIP) stations (Clauer et al., 2014), which were installed after the 2013 Saint Patrick's Day geomagnetic storm. Furthermore, Joule heating is most likely underestimated in GITM and the modeled values are almost independent between different storms, thus additional independent techniques of determining Joule heating are needed for the validation of both AMIE estimates and future modeling results (Verkhoglyadova et al., 2017). There are further, more general questions that remain unanswered, such as:

- To what extent does IMF $B_x$ play in generating interhemispheric asymmetries during geomagnetic storms?
- In what way does the preconditioning of GITM introduce asymmetries before the storm onset time and if these asymmetries exist are they realistic or unintentionally exaggerated?
- To what degree does the grid size used in these simulations need to be adjusted to create more accurate results, and what is the optimum spatiotemporal resolution for compatibility with drivers?

## 6. Conclusions

We have conducted a case study of the 2013 Saint Patrick's day geomagnetic storm using a global ionosphere thermosphere model (GITM) with both data-assimilated (AMIE) and empirical (Weimer-FRE) drivers. We focused on electromagnetic energy input, in the form of Joule heating and auroral heating, in the mid- and high-latitude regions of both hemispheres. We also considered the role asymmetric (over the geomagnetic hemispheres) solar insolation plays in asymmetric heating during this event at geographic equinox. The choice of data-assimilated driver is motivated by the desire to capture multi-scale physics, as well as to investigate interhemispheric asymmetries. To independently compare the simulations with two different drivers, we conduced data-model comparisons using Madrigal vertical TEC, GOCE vertical TEC and neutral density, and empirical CPCP formulas. The findings of the paper can be summarized as follows:

- Solar insolation has a significant effect on simulated hemispheric TEC, even at equinox.
- Asymmetric conductance profiles result in a diurnal variation in Joule and auroral heating aligned with solar insolation over the magnetic high-latitude regions.
- Realistic drivers perform better than or equivalent to empirical drivers in data-model comparison.
- Realistic drivers can produce more and intense localized heating events.
- TEC comparisons perform better in the Northern Hemisphere, potentially indicating sampling bias.

## Data Availability Statement

GITM can be found at (Ridley, 2021) and spacepy, a python package used to read GITM outputs, can be found at (Larsen et al., 2021). OMNI data can be found at (NASA, GSFC, 2021). The Madrigal GNSS TEC data can be found at (MIT Haystack, 2022). GOCE neutral density data can be found at (European Space Agency, 2009). Pickle files of the figures, underlying simulation result, codes used to generate figure and read the simulation output, and the AMIE files used to drive the simulations can be found in the FigShare (Smith et al., 2023).

**Acknowledgments**
This study makes use of NASA OMNI data and NOAA HPI data. The simulations were run on the Chinook Supercomputer at UAF. GITM is an open source code, developed by Aaron Ridley at the University of Michigan. The GITM output is processed using Spacepy package. The authors like to gratefully acknowledge all the data and model providers. The authors acknowledge the use of SuperDARN data. SuperDARN is a collection of radars funded by national scientific funding agencies of Australia, Canada, China, France, Italy, Japan, Norway, South Africa, United Kingdom and the United States of America. This work was sponsored by Guan Le though the NASA SESI Program. This research was supported by the International Space Science Institute (ISSI) in Bern, through the ISSI International Team project "Understanding Interhemispheric Asymmetry in MIT Coupling." AS work was supported by NASA SESI, NASA LWS Grant 4200749357, and NASA Grant 80NSSC20K1279. DSO work was also supported by NASA LWS Grant 4200749357. The work at New Jersey Institute of Technology was supported by NASA Grant 80NSSC21K0132 and NSF OPP-1744861. GL was supported in part by NASA Grants 80NSSC17K071 and 80NSSC21K1673.

## References

Banks, P., & Kockarts, G. (1973). *Aeronomy*. Academic Press.
Bilitza, D., Altadill, D., Truhlik, V., Shubin, V., Galkin, I., Reinisch, B., & Huang, X. (2017). International reference ionosphere 2016: From ionospheric climate to real-time weather predictions. *Space Weather*, *15*(2), 418–429. https://doi.org/10.1002/2016SW001593

Burns, A., Solomon, S., Wang, W., & Killeen, T. (2007). The ionospheric and thermospheric response to CMES: Challenges and successes. *Journal of Atmospheric and Solar-Terrestrial Physics*, *69*(1), 77–85. Challenges to Modeling the Sun-Earth System, a Workshop. https://doi.org/10.1016/j.jastp.2006.06.010

Cao, H., Russell, C. T., Christensen, U. R., Dougherty, M. K., & Burton, M. E. (2011). Saturn's very axisymmetric magnetic field: No detectable secular variation or tilt. *Earth and Planetary Science Letters*, *304*(1), 22–28. https://doi.org/10.1016/j.epsl.2011.02.035

Clauer, C. R., Kim, H., Deshpande, K., Xu, Z., Weimer, D., Musko, S., et al. (2014). An autonomous adaptive low-power instrument platform (AAL-PIP) for remote high-latitude geospace data collection. *Geoscientific Instrumentation, Methods and Data Systems*, *3*(2), 211–227. https://doi.org/10.5194/gi-3-211-2014

Codrescu, M. V., Fuller-Rowell, T. J., Foster, J. C., Holt, J. M., & Cariglia, S. J. (2000). Electric field variability associated with the millstone hill electric field model. *Journal of Geophysical Research*, *105*(A3), 5265–5273. https://doi.org/10.1029/1999ja900463

Cosgrove, R. B., & Codrescu, M. (2009). Electric field variability and model uncertainty: A classification of source terms in estimating the squared electric field from an electric field model. *Journal of Geophysical Research*, *114*(A6), A06301. https://doi.org/10.1029/2008JA013929

Dang, T., Lei, J., Wang, W., Wang, B., Zhang, B., Liu, J., et al. (2019). Formation of double tongues of ionization during the 17 march 2013 geomagnetic storm. *Journal of Geophysical Research: Space Physics*, *124*(12), 10619–10630. https://doi.org/10.1029/2019JA027268

Deng, Y., Fuller-Rowell, T. J., Akmaev, R. A., & Ridley, A. J. (2011). Impact of the altitudinal joule heating distribution on the thermosphere. *Journal of Geophysical Research*, *116*(A5), A05313. https://doi.org/10.1029/2010ja016019

Deng, Y., Heelis, R., Lyons, L. R., Nishimura, Y., & Gabrielse, C. (2019). Impact of flow bursts in the auroral zone on the ionosphere and thermosphere. *Journal of Geophysical Research: Space Physics*, *124*(12), 10459–10467. https://doi.org/10.1029/2019JA026755

Deng, Y., Richmond, A. D., Ridley, A. J., & Liu, H.-L. (2008). Assessment of the non-hydrostatic effect on the upper atmosphere using a general circulation model (GCM). *Geophysical Research Letters*, *35*(1), L01104. https://doi.org/10.1029/2007gl032182

Deng, Y., & Ridley, A. J. (2007). Possible reasons for underestimating joule heating in global models: E field variability, spatial resolution, and vertical velocity. *Journal of Geophysical Research*, *112*(A9), A09308. https://doi.org/10.1029/2006ja012006

Deng, Y., & Ridley, A. J. (2014). Simulation of non-hydrostatic gravity wave propagation in the upper atmosphere. *Annales Geophysicae*, *32*(4), 443–447. https://doi.org/10.5194/angeo-32-443-2014

Drob, D. P., Emmert, J. T., Meriwether, J. W., Makela, J. J., Doornbos, E., Conde, M., et al. (2015). An update to the horizontal wind model (HWM): The quiet time thermosphere. *Earth and Space Science*, *2*(7), 301–319. https://doi.org/10.1002/2014EA000089

European Space Agency. (2009). GOCE thermosphere data collection. version 1.0 [Dataset]. https://doi.org/10.5270/esa-l8g67jw

Fuller-Rowell, T. J., & Evans, D. S. (1987). Height-integrated Pedersen and Hall conductivity patterns inferred from the TIROS-NOAA satellite data. *Journal of Geophysical Research*, *92*(A7), 7606. https://doi.org/10.1029/ja092ia07p07606

Hedin, A. E., Salah, J. E., Evans, J. V., Reber, C. A., Newton, G. P., Spencer, N. W., et al. (1977). A global thermospheric model based on mass spectrometer and incoherent scatter data MSIS, 1. $N_2$ density and temperature. *Journal of Geophysical Research*, *82*(16), 2139–2147. https://doi.org/10.1029/JA082i016p02139

Heelis, R. A., & Maute, A. (2020). Challenges to understanding the Earth's ionosphere and thermosphere. *Journal of Geophysical Research: Space Physics*, *125*(7), e2019JA027497. https://doi.org/10.1029/2019ja027497

Hong, Y., Deng, Y., Zhu, Q., Maute, A., Sheng, C., Welling, D., & Lopez, R. (2021). Impacts of different causes on the inter-hemispheric asymmetry of ionosphere-thermosphere system at mid- and high-latitudes: GITM simulations. *Space Weather*, *19*(11), e2021SW002856. https://doi.org/10.1029/2021SW002856

Kalafatoglu Eyiguler, E. C., Kaymaz, Z., Frissell, N. A., Ruohoniemi, J. M., & Rastätter, L. (2018). Investigating upper atmospheric joule heating using cross-combination of data for two moderate substorm cases. *Space Weather*, *16*(8), 987–1012. https://doi.org/10.1029/2018SW001956

Knipp, D., Kilcommons, L., Hairston, M., & Coley, W. R. (2021). Hemispheric asymmetries in Poynting flux derived from DMSP spacecraft. *Geophysical Research Letters*, *48*(17), e2021GL094781. https://doi.org/10.1029/2021GL094781

Larsen, B. A., Morley, S. K., Niehof, J. T., & Welling, D. T. (2021). Spacepy [Dataset]. Zenodo. https://doi.org/10.5281/zenodo.3252523

Laundal, K. M., Cnossen, I., Milan, S. E., Haaland, S. E., Coxon, J., Pedatella, N. M., et al. (2016). North–South asymmetries in Earth's magnetic field. *Space Science Reviews*, *206*(1–4), 225–257. https://doi.org/10.1007/s11214-016-0273-0

Lin, C. Y., Deng, Y., Sheng, C., & Drob, D. P. (2017). A study of the nonlinear response of the upper atmosphere to episodic and stochastic acoustic-gravity wave forcing. *Journal of Geophysical Research: Space Physics*, *122*(1), 1178–1198. https://doi.org/10.1002/2016ja022930

Lu, G. (2017). Large scale high-latitude ionospheric electrodynamic fields and currents. *Space Science Reviews*, *206*(1–4), 431–450. https://doi.org/10.1007/s11214-016-0269-9

March, G., Doornbos, E., & Visser, P. (2019). High-fidelity geometry models for improving the consistency of CHAMP, GRACE, GOCE and Swarm thermospheric density data sets. *Advances in Space Research*, *63*(1), 213–238. https://doi.org/10.1016/j.asr.2018.07.009

March, G., Visser, T., Visser, P., & Doornbos, E. (2019). CHAMP and GOCE thermospheric wind characterization with improved gas-surface interactions modelling. *Advances in Space Research*, *64*(6), 1225–1242. https://doi.org/10.1016/j.asr.2019.06.023

McHarg, M., Chun, F., Knipp, D., Lu, G., Emery, B., & Ridley, A. (2005). High-latitude joule heating response to IMF inputs. *Journal of Geophysical Research*, *110*(A8), A08309. https://doi.org/10.1029/2004ja010949

Meng, X., & Verkhoglyadova, O. P. (2021). Quantifying contributions of external drivers to the global ionospheric state. *Space Weather*, *19*(9), e2021SW002752. https://doi.org/10.1029/2021sw002752

MIT Haystack. (2022). Madrigal GNSS tec [Dataset]. Retrieved from http://cedar.openmadrigal.org/

NASA, GSFC. (2021). Omni. [Dataset]. Retrieved from https://omniweb.gsfc.nasa.gov/form/omni_min.html

Ozturk, D. S., Meng, X., Verkhoglyadova, O. P., Varney, R. H., Reimer, A. S., & Semeter, J. L. (2020). A new framework to incorporate high-latitude input for mesoscale electrodynamics. *Journal of Geophysical Research: Space Physics*, *125*(1), e2019JA027562. https://doi.org/10.1029/2019JA027562

Pakhotin, I., Mann, I. R., Xie, K., Burchill, J., & Knudsen, D. (2020). Northern preference for terrestrial electromagnetic energy input from space weather. *Nature Communications*, *12*(199). https://doi.org/10.1002/essoar.10502993.1

Rees, M. H. (1989). *Physics and chemistry of the upper atmosphere*. Cambridge University Press.

Richmond, A. D. (1992). Assimilative mapping of ionospheric electrodynamics. *Advances in Space Research*, *12*(6), 59–68. https://doi.org/10.1016/0273-1177(92)90040-5

Richmond, A. D. (1995). Ionospheric electrodynamics using magnetic apex coordinates. *Journal of Geomagnetism and Geoelectricity*, *47*(2), 191–212. https://doi.org/10.5636/jgg.47.191

Richmond, A. D. (2011). Electrodynamics of ionosphere–thermosphere coupling. In M. A. Abdu, & D. Pancheva (Eds.), *Aeronomy of the Earth's atmosphere and ionosphere* (pp. 191–201). Springer Netherlands. https://doi.org/10.1007/978-94-007-0326-1_13

Rideout, W., & Coster, A. (2006). Automated GPS processing for global total electron content data. *GPS Solutions*, *10*(3), 219–228. https://doi.org/10.1007/s10291-006-0029-5

Ridley, A. J., Deng, Y., & Tóth, G. (2006). The global ionosphere–thermosphere model (GITM). *Journal of Atmospheric and Solar-Terrestrial Physics*, *68*(8), 839–864. https://doi.org/10.1016/j.jastp.2006.01.008

Ridley, A. J. (2005). A new formulation for the ionospheric cross polar cap potential including saturation effects. *Annales Geophysicae*, *23*(11), 3533–3547. https://doi.org/10.5194/angeo-23-3533-2005

Ridley, A. J. (2021). Global ionosphere/thermosphere model (GITM) [Software]. Retrieved from https://github.com/aaronjridley/GITM

Ridley, A. J., & Kihn, E. A. (2004). Polar cap index comparisons with AMIE cross polar cap potential, electric field, and polar cap area. *Geophysical Research Letters*, *31*(7), L07801. https://doi.org/10.1029/2003GL019113

Schunk, R. (1975). Transport equations for aeronomy. *Planetary and Space Science*, *23*(3), 437–485. https://doi.org/10.1016/0032-0633(75)90118-X

Shreedevi, P. R., Choudhary, R. K., Thampi, S. V., Yadav, S., Pant, T. K., Yu, Y., et al. (2020). Geomagnetic storm-induced plasma density enhancements in the southern polar ionospheric region: A comparative study using St. Patrick's Day storms of 2013 and 2015. *Space Weather*, *18*(8), e2019SW002383. https://doi.org/10.1029/2019SW002383

Smith, A. R., Ozturk, D. S., Delamere, P., Lu, G., & Kim, H. (2023). Investigating the interhemispheric asymmetry in joule heating during the 2013 St. Patrick's Day geomagnetic storm figshare [Dataset]. Retrieved from https://figshare.com/projects/IIAJHDSPDGS/163915

Thayer, J. P. (1998). Height-resolved joule heating rates in the high-latitude e region and the influence of neutral winds. *Journal of Geophysical Research*, *103*(A1), 471–487. https://doi.org/10.1029/97JA02536

Turner, N. E., Cramer, W. D., Earles, S. K., & Emery, B. A. (2009). Geoefficiency and energy partitioning in CIR-driven and CME-driven storms. *Journal of Atmospheric and Solar-Terrestrial Physics*, *71*(10), 1023–1031. (High Speed Solar Wind Streams and Geospace Interactions). https://doi.org/10.1016/j.jastp.2009.02.005

Verkhoglyadova, O. P., Meng, X., Mannucci, A. J., Mlynczak, M. G., Hunt, L. A., & Lu, G. (2017). Ionosphere-thermosphere energy budgets for the ICME storms of March 2013 and 2015 estimated with GITM and observational proxies. *Space Weather*, *15*(9), 1102–1124. https://doi.org/10.1002/2017sw001650

Vichare, G., Ridley, A., & Yiğit, E. (2012). Quiet-time low latitude ionospheric electrodynamics in the non-hydrostatic global ionosphere–thermosphere model. *Journal of Atmospheric and Solar-Terrestrial Physics*, *80*, 161–172. https://doi.org/10.1016/j.jastp.2012.01.009

Vierinen, J., Coster, A. J., Rideout, W. C., Erickson, P. J., & Norberg, J. (2015). Statistical framework for estimating GNSS bias. *Atmospheric Measurement Techniques Discussions*, *8*(9), 9373–9398. https://doi.org/10.5194/amtd-8-9373-2015

Weimer, D. R. (2005). Improved ionospheric electrodynamic models and application to calculating joule heating rates. *Journal of Geophysical Research*, *110*(A5), A05306. https://doi.org/10.1029/2004ja010884

Xu, Z., Hartinger, M. D., Clauer, C. R., Peek, T., & Behlke, R. (2017). A comparison of the ground magnetic responses during the 2013 and 2015 St. Patrick's Day geomagnetic storms. *Journal of Geophysical Research: Space Physics*, *122*(4), 4023–4036. https://doi.org/10.1002/2016ja023338

Yue, X., Wan, W., Liu, L., Liu, J., Zhang, S., Schreiner, W. S., et al. (2016). Mapping the conjugate and corotating storm-enhanced density during 17 March 2013 storm through data assimilation. *Journal of Geophysical Research: Space Physics*, *121*(12), 12202–12210. https://doi.org/10.1002/2016JA023038

Zhao, Y., Deng, Y., Wang, J., Zhang, S., & Lin, C. Y. (2020). Tropical cyclone-induced gravity wave perturbations in the upper atmosphere: GITM-R simulations. *Journal of Geophysical Research: Space Physics*, *125*(7), e2019JA027675. https://doi.org/10.1029/2019ja027675

Zhu, J., & Ridley, A. J. (2016). Investigating the performance of simplified neutral-ion collisional heating rate in a global it model. *Journal of Geophysical Research: Space Physics*, *121*(1), 578–588. https://doi.org/10.1002/2015JA021637

Zhu, Q., Deng, Y., Maute, A., Sheng, C., & Lin, C. Y. (2017). Impact of the vertical dynamics on the thermosphere at low and middle latitudes: GITM simulations. *Journal of Geophysical Research: Space Physics*, *122*(6), 6882–6891. https://doi.org/10.1002/2017ja023939

Zhu, Q., Lu, G., & Deng, Y. (2022). Low- and mid-latitude ionospheric response to the 2013 St. Patrick's Day geomagnetic storm in the American sector: Global ionosphere thermosphere model simulation. *Frontiers in Astronomy and Space Sciences*, *9*. https://doi.org/10.3389/fspas.2022.916739

Zhu, Q., Lu, G., Maute, A., Deng, Y., & Anderson, B. (2022). Assessment of using field-aligned currents to drive the global ionosphere thermosphere model: A case study for the 2013 St Patrick's Day geomagnetic storm. *Space Weather*, *20*(9), e2022SW003170. https://doi.org/10.1029/2022SW003170